Spontaneous patterns in coherently driven polariton microcavities

G. Díaz-Camacho, C. Tejedor, and F. M. Marchetti[*]

Departamento de Física Teórica de la Materia Condensada & Condensed Matter Physics Center (IFIMAC),
Universidad Autónoma de Madrid, Madrid 28049, Spain

We consider a polariton microcavity resonantly driven by two external lasers which simultaneously pump both lower and upper polariton branches at normal incidence. In this setup, we study the occurrence of instabilities of the pump-only solutions towards the spontaneous formation of patterns. Their appearance is a consequence of the spontaneous symmetry breaking of translational and rotational invariance due to interaction-induced parametric scattering. We observe the evolution between diverse patterns which can be classified as single pump, where parametric scattering occurs at the same energy as one of the pumps, and as two pump, where scattering occurs at a different energy. For two-pump instabilities, stripe and checkerboard patterns become the dominant steady-state solutions because cubic parametric scattering processes are forbidden. This contrasts with the single-pump case, where hexagonal patterns are the most common arrangements. We study the possibility of controlling the evolution between different patterns. Our results are obtained within a linear stability analysis and are confirmed by finite-size full numerical calculations.

I. INTRODUCTION

In recent years, hybrid matter-light systems such as microcavity polaritons have been proven ideal for the study of spontaneous pattern formation. Resulting from the strong coupling between cavity photons and quantum well excitons, microcavity polaritons share the properties of both components and, thus, display unique properties: among those, optical and electrical injection, a high degree of tunability and control, easy detection, and direct readout [1–3]. Optical parametric oscillation [4], where exciton-exciton interactions trigger parametric scattering from a pump state to a signal state at a lower momentum and energy and an idler state at a higher momentum and energy, is a paradigm of polariton spontaneous pattern formation. Here, dynamical patterns are generated by the interference between pump, signal, and idler states forming a stripelike pattern in real space. However, static geometrical patterns can be generated when parametric scattering spontaneously occurs from a pump state, e.g., at zero momentum, to two signal states at the same energy and opposite momenta. This instability was recently realized in triple [5] and double [6] cavities, as well as by blue-shifting the pump above the polariton dispersion in one-dimensional cavities [7,8]. For scattering at the same energy, scattering processes between pump and signal states of cubic order can lead to the formation of hexagonal patterns. This was predicted by Refs. [9–12] and experimentally realized in [13] using a double vertical cavity. Alternative patterns such as vortices and vortex lattices [14–16], vortex rings [17], and solitons [18] have also been investigated in polariton quantum fluids driven by a resonant pump. These have the additional benefit of carrying nontrivial phase configurations and, in case of vortices, a nonzero net angular momentum.

There is an analogy between optical patterns and Turing patterns, where spontaneous self-organized repetitive spatial configurations emerge out of a homogeneous distribution. Turing patterns were first proposed in the context of chemical reactions [19], and, since then, used to describe a wide range of patterns in diverse fields [20], such as in animal coats, skin pigmentation, and ridges on sand dunes. The common features of Turing patterns are nonlocality, such as diffusion, and nonlinear interactions. Diffusion promotes homogeneity, yet, when the system is driven externally by, e.g., stress, instabilities with certain preferred wavelengths can grow exponentially because of the nonlinearities. With a similar mechanism, Turing patterns can occur in nonlinear optical systems, such as nonlinear media embedded in optical resonators [21].

In this paper, we consider a polariton microcavity resonantly driven by two external lasers which simultaneously pump both lower and upper polariton branches at normal incidence so as not to explicitly break the system translational and rotational invariance (see schematic Fig. 1). This pumping setup was already suggested as a possible scheme for the generation of entangled multiple polariton modes [22]. More recently, a simpler but similar configuration was proposed in the context of quantum exciton-polariton networks [23]: here, an inverse four-wave mixing procedure practically implements a two-mode squeezing Hamiltonian. However, the nature and stability of different patterns following the spontaneous breaking of translational and rotational symmetry due to parametric scattering has not been analyzed yet. The aim of our work is the study of those patterns that can be generated by this pumping scheme and the control over them in terms of the system parameters.

By complementing the results of a linear stability analysis with numerical simulations for finite-size pump profiles, we observe the evolution between diverse patterns which can be classified as "single pump" (where parametric scattering occurs at the same energy as one of the pumps) and as "two pump"
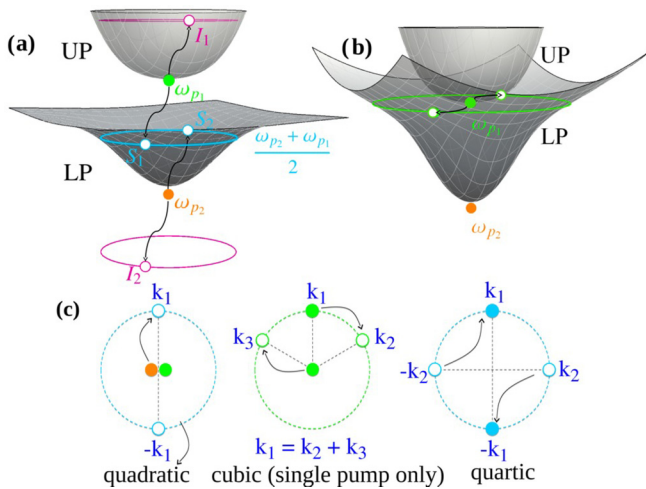
_____
[*]francesca.marchetti@uam.es

FIG. 1. Schematic representation of the pumping configuration and main scattering processes leading to two-pump (a) and single-pump (b) instabilities. (a) Two driving laser fields are tuned at zero momentum almost resonantly with the upper polariton (UP) at ω_{p_1} (green dot) and lower polariton (LP) at ω_{p_2} (orange dot); UP and LP energy-momentum dispersions are plotted as (gray) surfaces. Interactions between the two-pump states as well as in within each single-pump state trigger scattering [(black) arrows] from the pump states to signal $S_{1,2}$ (cyan) and idler $I_{1,2}$ (magenta) states. Panel (b) describes the fixed-energy parametric scattering, which is allowed when the interaction renormalization of the dispersion admits LP states at the pump energy ω_{p_1}. (c) Quadratic and quartic scattering processes are permitted for both two-pump (a) and single-pump (b) instabilities, while cubic processes are forbidden when pump and signal states are at different energies (a).

(where scattering occurs at an energy equal to the average of the two-pump energies). For two-pump instabilities, stripe and checkerboard patterns become the dominant steady-state solutions because cubic parametric scattering processes are forbidden when pumps and signals are at different energies, as schematically depicted in Fig. 1. This contrasts with the single-pump case, where, because of cubic order processes, hexagonal patterns are the most common instabilities [9–13].

In a "phase diagram" of momentum versus pump power, we establish the regions of instability of the pump-only solutions, i.e., those configurations for which only the states resonantly injected by the external pumps are populated. At the same time, we estimate, as a function of the pump strength, the absolute value of the momentum typical of each instability. The values extracted from the numerical simulations agree very well with the values found for the most unstable modes derived within the linear stability analysis, as well as with an estimate obtained by a simplified description of the interaction-induced renormalization of the bare dispersion branches. In particular, we establish that the phase diagram is composed by different branches which can be explained in terms of both the blue-shift and the splitting induced by the interaction between the two-pump states mediated by excitons. Among the two-pump instabilities, checkerboard patterns typically occur at low pump powers. Contrary to expectations, we do not have a clear evolution from stripes at the lowest pump powers to checkerboards at higher pump strength. Rather, we

obtain that these instabilities alternate at low pump powers until, eventually, only stripe solutions are allowed at very high pump powers.

If no single-pump instabilities develop, the momentum typical of these patterns decreases monotonously as a function of the pump strength. However, two-pump instabilities can compete with single-pump ones, when the energy of the pump which is tuned close to the upper polariton branch becomes resonant with the interaction-renormalized lower polariton branches. This can lead to the formation of hexagonal patterns because of parametric scattering at the same energy, while the system can also sustain two-pump scattering processes which instead promote the formation of stripe and checkerboard patterns. We can demonstrate the competition between single- and two-pump instabilities by filtering the emission in energy, showing that the system simultaneously undergoes different instabilities at different energies.

Finally, we have studied the phase freedom of two-pump instabilities. In spite of the coherent nature of the two driving laser pumps, we demonstrate that the system is characterized by phase freedom. In particular, the number of independent phase constraints imposed by parametric scattering processes from the pump to the signal and idler states is always less than the number of generated signal and idler modes. We show that the system spontaneously chooses the relative phase between opposite momentum signals (which coincide with the relative phase of opposite momentum idlers). Thus, a U(1) phase symmetry is spontaneously broken in the case of stripe patterns, while for checkerboard the phase symmetry spontaneously broken is in the U(1) × U(1) class.

Phase freedom opens the possibility of realizing macro-scopic phase coherent states and of investigating their super-fluid behavior. These aspects have been recently analyzed for optical parametric oscillation, either by studying the current persistence [24,25] or by probing the system response to the scattering against a defect [26]. Further, because of the different continuous symmetry characterizing stripe and checkerboard patterns, it would be interesting to study first-order correlation functions both in space and time so as to establish the critical behavior of this nonequilibrium two-dimensional system and the class of nonequilibrium phase transition to which it belongs [27]. In addition, higher-order correlations would give indications of a possible quantum behavior [22,23,28,29].

The paper is organized as follows: The model and the pumping scheme, as well as the relevant scattering processes, are introduced in Secs. II and II A. The choice of the system parameters that are optimal for the analysis of two-pump pattern formation is discussed in Sec. II B. In Sec. III we present the results derived within a linear response theory, while these are compared to the results obtained with finite-size numerical simulations in Sec. IV. We argue about the system phase freedom in Sec. IV A. Finally, conclusions and perspectives form Sec. V.

II. MODEL

We describe the dynamics of microcavity polaritons reso-nantly driven by two continuous-wave laser fields shined at normal incidence ($\mathbf{k}_{p_1} = 0 = \mathbf{k}_{p_2}$)

$$F(\mathbf{r},t) = f_{p_1}(\mathbf{r})e^{-i\omega_{p_1}t} + f_{p_2}(\mathbf{r})e^{-i\omega_{p_2}t} \tag{1}$$

by a Gross-Pitaevskii equation for coupled cavity [$\psi_C(\mathbf{r},t)$] and exciton [$\psi_X(\mathbf{r},t)$] fields generalized to include decay and resonant pumping ($\hbar = 1$) [30,31]:

$$i\partial_t \begin{pmatrix} \psi_X \\ \psi_C \end{pmatrix} = \begin{pmatrix} 0 \\ F \end{pmatrix} + \left[\hat{H}_0 + \begin{pmatrix} g_X|\psi_X|^2 & 0 \\ 0 & 0 \end{pmatrix} \right] \begin{pmatrix} \psi_X \\ \psi_C \end{pmatrix}, \quad (2)$$

where the single-polariton Hamiltonian is given by

$$\hat{H}_0 = \begin{pmatrix} \omega_{X,-i\nabla} - i\kappa_X & \Omega_R/2 \\ \Omega_R/2 & \omega_{C,-i\nabla} - i\kappa_C \end{pmatrix}. \quad (3)$$

Here, we assume the cavity dispersion to be quadratic, $\omega_{C,\mathbf{k}} = \omega_{C,\mathbf{0}} + k^2/(2m_C)$, with $m_C = 10^{-5}m_0$ (m_0 is the bare electron mass),while we will neglect the exciton dispersion $\omega_{X,\mathbf{k}} = \omega_{X,\mathbf{0}}$ as the exciton mass is much larger than the cavity photon mass, typically $m_X \simeq 0.4m_0$. Energies will be measured with respect to the exciton one, $\omega_{X,\mathbf{0}}$, and we define the photon-exciton detuning as $\delta = \omega_{C,\mathbf{0}} - \omega_{X,\mathbf{0}}$. Exciton and photon fields are coupled through the Rabi splitting Ω_R. The exciton-exciton interaction is approximated as a contact interaction of strength g_X. This approximation follows from the fact that the typical range of exciton-exciton interaction is of the order of the Bohr radius $a_B \sim$ nm, and this length is much smaller than typical polariton wavelengths $\ell = 1/\sqrt{m_C\Omega_R} \sim \mu$m. Note that the value of the interaction strength g_X does not influence the dynamics, as its dependence can be rescaled out from Eqs. (2) by defining $\tilde{\psi}_{X,C} = \sqrt{g_X}\psi_{X,C}$ and $\tilde{f}_{p_{1,2}} = \sqrt{g_X}f_{p_{1,2}}$. Finally, κ_X and κ_C are the exciton and photon decay rates.

A. Two-pump instabilities

We briefly describe in this section the main scattering processes that characterize single- and two-pump parametric instabilities with the scope of schematically illustrating which patterns are promoted by each process. The exciton-exciton interaction term inducing scattering in the generalized Gross-Pitaevskii equation (2) can be derived from a many-body action written in terms of the exciton field $\psi_X(\mathbf{r},t)$:

$$\mathcal{S}_{int} = \frac{g_X}{2} \int dt \int d\mathbf{r} |\psi_X(\mathbf{r},t)|^4. \quad (4)$$

This expression is local both in space $\mathbf{r}$ as well as in time t, which implies that the only scattering processes allowed are those that simultaneously conserve energy and momentum. We assume that, aside from the pump states resonantly injected by the external lasers ($\omega_{p_1}, \mathbf{k}_{p_1} = \mathbf{0}$) and ($\omega_{p_2}, \mathbf{k}_{p_2} = \mathbf{0}$), the interaction allows the population of other states. These are indicated as signal and idler states in Fig. 1(a). However, here, in a simplified formulation, we assume that only signal states with energy ω_s and different possible momenta $\mathbf{k}$ can be populated:

$$\psi_X(\mathbf{r},t) = \sum_{i=1,2} P_{iX}e^{-i\omega_{p_i}t} + e^{-i\omega_s t}\sum_{\mathbf{k}} S_{\mathbf{k}}e^{-i\mathbf{k}\cdot\mathbf{r}}.$$

Assuming that only the pump states are macroscopically occupied and perturbatively expanding in the additional signal states leads, as explained in Sec. III, to the linear response theory. This approximation scheme allows to ascertain the stability of the pump-only solutions. However, by keeping in the expansion of the action $\mathcal{S}_{int}$ all the terms in $S_{\mathbf{k}}$, we can

describe the scattering processes illustrated in Fig. 1(c) which are those responsible for the selection of specific patterns.

In particular, the second-order term

$$\mathcal{S}_{int}^{(2)} = g_X P_{1X} P_{2X} \sum_{\mathbf{k}} S_{\mathbf{k}}^* S_{-\mathbf{k}}^* \delta_{\omega_{p_1}+\omega_{p_2},2\omega_s}$$

describes the quadratic process which populates the signal energy $\omega_s = (\omega_{p_1} + \omega_{p_2})/2$ and promotes the population of opposite momentum states, i.e., stripe formation. This process is allowed for both cases where either two pumps or a single pump are present, the difference in this last case is that scattering is only allowed when the signal states are at the same energy as the pump. Because of energy conservation, third-order processes are allowed only for single-pump instabilities, i.e., for

$$\mathcal{S}_{int}^{(3)} = g_X P_{1X} \sum_{\mathbf{k}_1,\mathbf{k}_2,\mathbf{k}_3} S_{\mathbf{k}_1} S_{\mathbf{k}_2}^* S_{\mathbf{k}_3}^* \delta_{\mathbf{k}_1,\mathbf{k}_2+\mathbf{k}_3} \delta_{\omega_{p_1},\omega_s}.$$

Because of the system rotational symmetry, the signal momenta $\mathbf{k}_i$ have all to lie on the same circle, i.e., have the same moduli. For this reason, $-\mathbf{k}_1, \mathbf{k}_2$, and $\mathbf{k}_3$ in the expression above are arranged on a equilateral triangle and, thus, third-order processes promote hexagonal patterns. Finally, the fourth-order process

$$\mathcal{S}_{int}^{(4)} = \frac{g_X}{2} \sum_{\mathbf{k}_1,\mathbf{k}_2,\mathbf{k}_3,\mathbf{k}_4} S_{\mathbf{k}_1} S_{\mathbf{k}_2} S_{\mathbf{k}_3}^* S_{\mathbf{k}_4}^* \delta_{\mathbf{k}_1+\mathbf{k}_2,\mathbf{k}_3+\mathbf{k}_4}$$

populates pairs of opposite momenta states that, when arranged at 90°, generate checkerboard, and, for any other angle, produce rhombic patterns. Note that this argument does not give any preference towards checkerboard patterns with perpendicular orientation over rhombiclike structures. However, in the following, in our numerical simulations we will only derive squared checkerboards.

If the two-pump frequencies ω_{p_1} and ω_{p_2} are tuned close to the upper (UP) and lower polariton (LP) branches, respectively, then the system parameters can be chosen so as to have the signal energy $\omega_s = (\omega_{p_1} + \omega_{p_2})/2$ relative to two-pump processes resonant with the LP branch at a specific momentum. The absence of third-order processes in two-pump parametric scattering guarantees that other patterns than the hexagonal ones, such as stripe and checkerboard, can be realized. Interestingly, there is an analogy between the pattern formation mechanisms described for our typically nonequilibrium system and the theory of weak crystallization, which is an equilibrium theory and thus follows the principle of energy minimization. This is briefly discussed in the Appendix. In the next section, we describe the optimal choice of parameters that leads to a large two-pump instability region.

B. Choice of parameters

In absence of interactions, the single-polariton Hamiltonian $\hat{H}_0$ can be diagonalized in momentum space by rotating into the lower (LP) and upper polariton (UP) basis,

$$\begin{pmatrix} \psi_{LP}(\mathbf{k}) \\ \psi_{UP}(\mathbf{k}) \end{pmatrix} = \begin{pmatrix} \cos\theta_{\mathbf{k}} & \sin\theta_{\mathbf{k}} \\ -\sin\theta_{\mathbf{k}} & \cos\theta_{\mathbf{k}} \end{pmatrix} \begin{pmatrix} \psi_X(\mathbf{k}) \\ \psi_C(\mathbf{k}) \end{pmatrix}, \quad (5)$$

TABLE I. Choice of the system parameters.

	Case A	Case B
m_C (m_0)		10^{-5}
Ω_R (meV)		10
δ (meV)		-5
$\omega_{p_1} - \omega_{X,0}$ (meV)		3.05
Δ_{p_1} (meV)		-0.04
$\omega_{p_2} - \omega_{X,0}$ (meV)	-9.0	-8.5
Δ_{p_2} (meV)	-0.91	-0.41
$\kappa_X = \kappa_C$ (meV)	0.3	0.4

to give the LP and UP branches (see top panels of Fig. 1):

$$\omega_{\text{LP,UP},\mathbf{k}} = \frac{\omega_{X,0} + \omega_{C,\mathbf{k}}}{2} \mp \frac{\sqrt{[\omega_{C,\mathbf{k}} - \omega_{X,0}]^2 + \Omega_R^2}}{2}. \quad (6)$$

The Rabi splitting Ω_R and the photon-exciton detuning δ determine the photon and exciton percentage that LP and UP have along their dispersion, i.e., the Hopfield factors:

$$\begin{matrix} \cos^2 \theta_{\mathbf{k}} \\ \sin^2 \theta_{\mathbf{k}} \end{matrix} = \frac{1}{2} \left[1 \pm \frac{\omega_{C,\mathbf{k}} - \omega_{X,0}}{\sqrt{[\omega_{C,\mathbf{k}} - \omega_{X,0}]^2 + \Omega_R^2}} \right]. \quad (7)$$

We rescale each overall pump strength differently, according to

$$f_{p_1}(\mathbf{r}) = \sin \theta_0 F_p(\mathbf{r}), \quad f_{p_2}(\mathbf{r}) = \cos \theta_0 F_p(\mathbf{r}). \quad (8)$$

This condition approximatively guarantees that, for a fixed value of F_p, each pump injects the same density of UPs at ω_{p_1} and LPs at ω_{p_2}. This condition is only approximatively guaranteed because, as soon as the pump strength is finite, UPs and LPs are affected by different blue-shifts and thus their photon fraction is not determined by the Hopfield factors, which instead refer to the bare LP and UP dispersions.

We fix the Rabi splitting to $\Omega_R = 10$ meV, a value available in GaAs-based structures. For this value, $\ell = 1/\sqrt{m_C \Omega_R} \simeq 0.58$ μm. The other microcavity parameters, such as δ and $\kappa_{X,C}$, as well as the pump frequencies $\omega_{p_{1,2}}$, are chosen so as to maximize the region of the two-pump instability [see Fig. 1(a)]. Clearly, such a scattering is not allowed at positive detunings, for which $\omega_{\text{LP},0} + \omega_{\text{UP},0} > 2\omega_{X,0}$. We thus choose a negative value for the detuning $\delta = -5$ meV, which we will see in the next section guarantees a large region of two-pump parametric instability.

The pump frequencies $\omega_{p_{1,2}}$ are chosen so as to eliminate the possibility of bistable behavior of each pump separately [32]. When both frequencies are red-detuned just below the UP and LP dispersions, i.e., when the pump detunings

$$\Delta_{p_1} = \omega_{p_1} - \omega_{\text{UP},0}, \quad \Delta_{p_2} = \omega_{p_2} - \omega_{\text{LP},0} \quad (9)$$

are negative, the populations of these states grow monotonically as a function of each pump intensity, a regime known as optical limiter.

In the following, we consider two specific choice parameters specified in Table I. As explained in the next section, by carrying on a linear response approximation, we have determined that these parameters are optimal in order to observe two-pump instabilities. Note that the chosen values of the

exciton and photon decay are larger than those in currently available cavities, even more so for the state-of-the-art high-Q microcavities which have been recently grown [33]. Clearly, decreasing the quality of a cavity is not difficult to achieve. As discussed in detail later on, we find that the chosen values of the decays are optimal for having a large region of two-pump instabilities and, at the same time, for guaranteeing a fast convergence of two-pump patterns to a steady-state solution.

III. LINEAR RESPONSE THEORY

For homogeneous pumping $F_p(\mathbf{r}) = F_p$, we can evaluate the region of instability of the pump-only solutions by applying a linear response approximation [34]. Here, the two-pump states $P_{i\alpha}$ (where $i = 1,2$ indicates the pump component and $\alpha = X,C$ indicates the excitonic and photonic component) are macroscopically occupied, while signal ($S_{i\alpha}$) and idler ($I_{i\alpha}$) terms are treated perturbatively:

$$\begin{aligned} \psi_\alpha(\mathbf{r},t) = {}& e^{-i\omega_{p_1}t} P_{1\alpha} + e^{-i\omega_{p_2}t} P_{2\alpha} \\ & + e^{-i\omega_{p_1}t} \sum_{\mathbf{k}} [I_{1\alpha,\mathbf{k}} e^{i(\mathbf{k}\cdot\mathbf{r}-\omega t)} + S_{1\alpha,\mathbf{k}}^* e^{-i(\mathbf{k}\cdot\mathbf{r}-\omega t)}] \\ & + e^{-i\omega_{p_2}t} \sum_{\mathbf{k}} [S_{2\alpha,\mathbf{k}} e^{i(\mathbf{k}\cdot\mathbf{r}-\omega t)} + I_{2\alpha,\mathbf{k}}^* e^{-i(\mathbf{k}\cdot\mathbf{r}-\omega t)}]. \end{aligned}$$

$$(10)$$

The notation is the same one of Fig. 1(a): Pump 1 scatters at higher energy $\omega_{p_1} + \omega$ into the idler state $I_{1\alpha}$ and at lower energy $\omega_{p_1} - \omega$ into the signal state $S_{1\alpha}$, while pump 2 scatters at higher energy $\omega_{p_2} + \omega$ into the signal state $S_{2\alpha}$ and at lower energy $\omega_{p_2} - \omega$ into the idler state $I_{2\alpha}$.

Substituting this ansatz into the equation of motion (2), one obtains, at zeroth order, i.e., neglecting the signal and idler contributions, four mean-field equations for the pump states [35]:

$$(\omega_{X,0} - \omega_{p_1} - i\kappa_X + G_{12}) P_{1X} + \frac{\Omega_R}{2} P_{1C} = 0,$$

$$(\omega_{C,0} - \omega_{p_1} - i\kappa_C) P_{1C} + \frac{\Omega_R}{2} P_{1X} + f_{p_1} = 0,$$

$$(\omega_{X,0} - \omega_{p_2} - i\kappa_X + G_{21}) P_{2X} + \frac{\Omega_R}{2} P_{2C} = 0,$$

$$(\omega_{C,0} - \omega_{p_2} - i\kappa_C) P_{2C} + \frac{\Omega_R}{2} P_{2X} + f_{p_2} = 0, \quad (11)$$

where $G_{ij} = g_X(|P_{iX}|^2 + 2|P_{jX}|^2)$. The same equations have been already solved in Ref. [35] to demonstrate that two pumping lasers can lead to tunable multistable hysteresis cycles with up to three stable pump-only solutions. Here, in this work, we want to avoid multistable regimes as they might compete with the two-pump instability described in Fig. 1(a). For this reason, we choose negative values for the pump detunings (9), a necessary condition to guarantee the optical limiter regime. In fact, as later shown in the bottom panels of Figs. 3 and 4, for our choice of parameters A and B (see Table I), the pump states $P_{i\alpha}$ grow monotonously as a function of the pump strength F_p. In particular, in these figures, we plot the total exciton density in the pump states $n_X^{\text{tot}} = |P_{1X}|^2 + |P_{2X}|^2$.

Expanding (2) to the first order in the signal and idler terms, we can carry on a linear stability analysis of the pump-only

solutions of (11): the formalism is the same as the erratum of Ref. [36]. In this expansion, one only keeps the terms oscillating with frequencies $\omega_{p_i} \pm \omega$, while terms oscillating with frequencies $2\omega_{p_i} - \omega_{p_j} \pm \omega$ are neglected. As a result, one obtains the eigenvalue equation $\mathcal{L}_\mathbf{k} W_\mathbf{k} = \omega W_\mathbf{k}$ (diagonal in momentum space) for the eight-component eigenvector

$$W_\mathbf{k}^T = (\underbrace{I_{1X,\mathbf{k}}, I_{1C,\mathbf{k}}}_{p}, \underbrace{S_{1X,\mathbf{k}}, S_{1C,\mathbf{k}}}_{h}, \underbrace{S_{2X,\mathbf{k}}, S_{2C,\mathbf{k}}}_{p}, \underbrace{I_{2X,\mathbf{k}}, I_{2C,\mathbf{k}}}_{h}),$$

where we have explicitly indicated the particlelike ($I_{1\alpha,\mathbf{k}}$ and $S_{2\alpha,\mathbf{k}}$) and holelike ($S_{1\alpha,\mathbf{k}}$ and $I_{2\alpha,\mathbf{k}}$) components. The Bogoliubov matrix $\mathcal{L}_\mathbf{k}$,

$$\mathcal{L}_\mathbf{k} = \begin{pmatrix} \mathbb{L}_{\mathbf{k}11} & \mathbb{L}_{\mathbf{k}12} \\ \mathbb{L}_{\mathbf{k}21} & \mathbb{L}_{\mathbf{k}22} \end{pmatrix}, \qquad (12)$$

can be decomposed in terms of the pump index block-diagonal terms

$$\mathbb{L}_{\mathbf{k}ii} = \begin{pmatrix} E_{iX,\mathbf{k}} & \frac{\Omega_R}{2} & g_X P_{iX}^2 & 0 \\ \frac{\Omega_R}{2} & E_{iC,\mathbf{k}} & 0 & 0 \\ -g_X P_{iX}^{*\,2} & 0 & -E_{iX,\mathbf{k}}^* & -\frac{\Omega_R}{2} \\ 0 & 0 & -\frac{\Omega_R}{2} & -E_{iC,\mathbf{k}}^* \end{pmatrix},$$

where

$$E_{iX,\mathbf{k}} = \omega_{X,\mathbf{k}} - \omega_{p_i} + 2g_X n_X^{\text{tot}} - i\kappa_X,$$

$$E_{iC,\mathbf{k}} = \omega_{C,\mathbf{k}} - \omega_{p_i} - i\kappa_C,$$

and $n_X^{\text{tot}} = |P_{1X}|^2 + |P_{2X}|^2$, and in terms of the off-diagonal terms

$$\mathbb{L}_{\mathbf{k}i \neq j} = 2g_X \begin{pmatrix} P_{iX} P_{jX}^* & 0 & P_{iX} P_{jX} & 0 \\ 0 & 0 & 0 & 0 \\ -P_{iX}^* P_{jX}^* & 0 & -P_{iX}^* P_{jX} & 0 \\ 0 & 0 & 0 & 0 \end{pmatrix}.$$

The eigenvalues of $\mathcal{L}$ give the eight branches for the complex spectrum of excitation $\omega_\mathbf{k}^{(n)}$. The $n = 1, \ldots, 8$ branches can be labeled by the pump $i = 1,2$ index, the excitonic and photonic index $\alpha = X,C$, and the particle-hole $\ell = p,h$ index. In fact, in the $k \to \infty$ limit, one recovers the rescaled exciton and photon dispersions and thus one can associate to each of the eight branches one specific value of these three indices according to

$$\lim_{k \to \infty} \omega_\mathbf{k}^{(i,X,\ell)} \simeq \sigma_\ell \Bigg[\omega_{X,\mathbf{k}} + 2g_X n_X^{\text{tot}} - \omega_s$$

$$- \sigma_i \sqrt{\left(2g_X n_X^{\text{tot}}\right)^2 + \left(\frac{\omega_{p_1} - \omega_{p_2}}{2}\right)^2} \Bigg] - i\kappa_X,$$

where $\omega_s = (\omega_{p_1} + \omega_{p_2})/2$ and

$$\lim_{k \to \infty} \omega_\mathbf{k}^{(i,C,\ell)} \simeq \sigma_\ell (\omega_{C,\mathbf{k}} - \omega_{p_i}) - i\kappa_C,$$

where the sign $\sigma_\ell = \pm$ corresponds to the particle and hole branches $\ell = p,h$, respectively and the sign $\sigma_i = \pm$ refers to the pump index $i = 1,2$. These expressions have been derived by neglecting the pairing terms between the particle and hole degrees of freedom and thus are approximate and only valid at low pump powers. Note, however, that each branch is in general
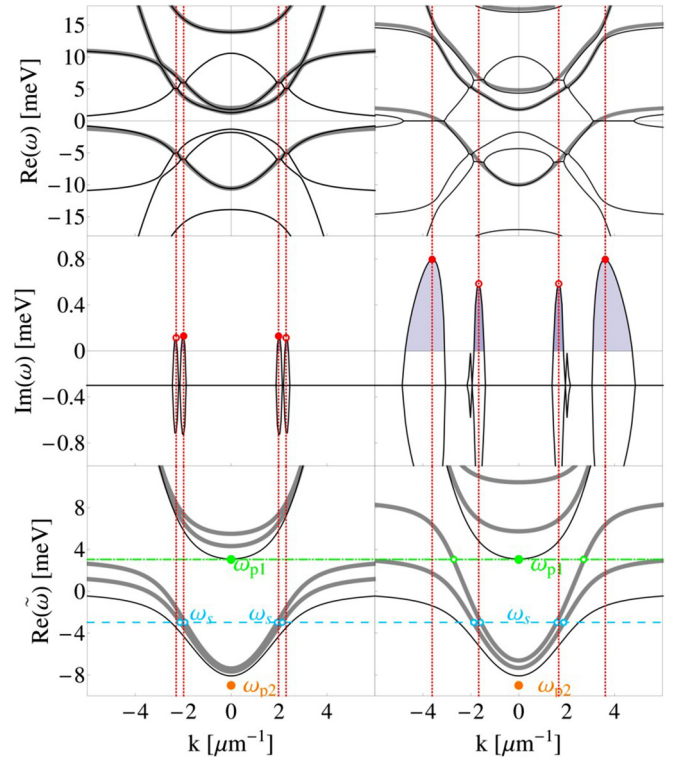

FIG. 2. Upper panels: the real part of the excitation spectrum $\text{Re}(\omega_\mathbf{k}^{(i,\alpha,\ell)})$ [thin (black) lines], where its eight branches can be labeled by the pump $i = 1,2$ index, the excitonic and photonic index $\alpha = X,C$, and the particle-hole $\ell = p,h$ index (see text). The real part of the simplified particlelike excitation spectrum, resulting from the diagonalization of (13), where we have neglected the particle-hole coupling terms, have been plotted as thick (gray) lines. Middle panels: imaginary part of the spectrum of excitations $\text{Im}(\omega_\mathbf{k}^{(i,\alpha,\ell)})$. Gray shaded regions indicate the unstable models for which $\text{Im}(\omega_\mathbf{k}^{(i,\alpha,\ell)}) > 0$. The (red) vertical dotted lines mark the momenta of the most unstable modes. Bottom panels: the interaction-renormalized LP and UP dispersions [thick (gray) lines] show that, at finite values of the pump strength, the interaction between the two-pump states in the particle-particle channel induces a blue-shift and a splitting of both the LP and the UP bare dispersions [(black) thin lines]. The dashed (cyan) line indicates the energy of the signal $\omega_s = (\omega_{p_1} + \omega_{p_2})/2$ expected for the two-pump instability, while the dotted-dashed (green) line indicates the pump-1 energy ω_{p_1} at which one can have scattering at large enough values of F_p (right panels). In all panels, the choice of parameters corresponds to the case A described in Table I, while the pump strength has been fixed to $\sqrt{g_X} F_p = 2.79$ meV$^{3/2}$ (left panels) and to $\sqrt{g_X} F_p = 11.18$ meV$^{3/2}$ (right panels).

characterized by the "particle-hole" symmetry $\omega_{-\mathbf{k}}^{(n)} = -\omega_\mathbf{k}^{(n)*}$, which is a consequence of the symmetry of $\mathcal{L}$.

The real part of the excitation spectrum $\text{Re}(\omega_\mathbf{k}^{(i,\alpha,\ell)})$ gives information about the renormalization of the LP and UP bare dispersions induced by the interaction between excitons. We plot the real part of the entire spectrum with its eight branches in the top panel of Fig. 2 [thin (black) lines] for two values of the pump power; the system parameters for this figure correspond to the case A described in Table I. We can observe that the "particle-hole" symmetry is satisfied. Further, one can observe that there are intervals in momenta for which particlelike

branches "stick together" with holelike branches. This is due to the anomalous terms in the Bogoliubov matrix characterizing the coupling between the particle and hole degrees of freedom which induce a nontrivial (i.e., different from $-\kappa_X$ and $-\kappa_C$) imaginary part of the spectrum $\text{Im}(\omega_{\mathbf{k}}^{(i,\alpha,\ell)})$ (middle panel of Fig. 2).

While crucial for determining the imaginary part of the spectrum, as discussed later, these anomalous terms can be safely neglected if one needs a simplified yet approximated information about the interaction-induced blue-shift of the LP and UP dispersions. To show this, we consider a reduced version of the Bogoliubov matrix where we neglect the coupling terms between the particle and hole degrees of freedom and consider the particle-particle components only:

$$\tilde{\mathbb{L}}_{\mathbf{k}} = \begin{pmatrix} E_{1X,\mathbf{k}} & \frac{\Omega_R}{2} & 2g_X P_{1X} P_{2X}^* & 0 \\ \frac{\Omega_R}{2} & E_{1C,\mathbf{k}} & 0 & 0 \\ 2g_X P_{2X} P_{1X}^* & 0 & E_{2X,\mathbf{k}} & \frac{\Omega_R}{2} \\ 0 & 0 & \frac{\Omega_R}{2} & E_{2C,\mathbf{k}} \end{pmatrix}. \quad (13)$$

In the top panel of Fig. 2 we plot as thick (gray) lines the real part of the four corresponding particlelike branches obtained by diagonalizing $\tilde{\mathbb{L}}_{\mathbf{k}}$. Note that the imaginary part of the eigenvalues of $\tilde{\mathbb{L}}_{\mathbf{k}}$ consists solely of the decay terms, i.e., either $-\kappa_X$ or $-\kappa_C$, depending on the branch one refers to. From these plots we can appreciate that, as soon as the external pumps induce finite values of both pump fields $P_{i\alpha}$, i.e., as soon as $F_p \neq 0$, the interaction between the two-pump states in the particle-particle channel $2g_X P_{1X} P_{2X}^*$ induces a splitting of the LP and UP branches, resulting in a total of four particle branches. In addition, each branch is blue-shifted because of the $2g_X n_X^{\text{tot}}$ term in the diagonal components $E_{i\alpha,\mathbf{k}}$ of the Bogoliubov matrix. Note that, according to the definition (10), the frequency ω characterizing the excitation spectrum is the frequency measured with respect to either pump frequency ω_{p_1} or ω_{p_2}. Thus, in order to characterize the splitting and blue-shift of the LP and UP bare dispersions [thin (black) lines in the bottom panels of Fig. 2] induced by the interaction, we set to zero the terms in ω_{p_1} and ω_{p_2} in the diagonal components $E_{i\alpha,\mathbf{k}}$ of the simplified Bogoliubov matrix $\tilde{\mathbb{L}}_{\mathbf{k}}$ (13) and plot the corresponding eigenvalues $\tilde{\omega}_{\mathbf{k}}^{(i,\alpha)}$ in the bottom panels of Fig. 2 as thick (gray) lines. Thus, we can quantify the splitting and blue-shift of the bare LP and UP modes. In addition, we can describe how both splitting and blue-shift grow when increasing the pump power F_p (from the left to the right panel).

This estimate of the interaction-renormalized dispersions allows to deduce the approximate values of the expected momenta for both two-pump as well as single-pump instabilities. To this end, in the bottom panels of Fig. 2 we plot as a dashed (cyan) line the value of the two-pump signal energy $\omega_s = (\omega_{p_1} + \omega_{p_2})/2$. Because of the splitting of the LP mode, we obtain in this way two values of the expected two-pump instability momenta. While at low enough pump powers (as for the left panels of Fig. 2), the blue-shift of the LP is not large enough to get any LP state at the pump-1 energy ω_{p_1} [dotted-dashed (green) line], for big enough values of F_p (right panels) the blue-shift of at least one split LP branch is large enough to allow single-pump parametric scattering. As discussed next, the values obtained this way for both

two-pump and single-pump instability momenta are close to those obtained evaluating the imaginary part of the spectrum and the most unstable modes.

An additional and better estimate of the momenta at which we expect two-pump and single-pump instabilities to occur can be obtained by evaluating the most unstable modes. The pump-only solutions of the mean-field equations (11) are stable as far as the population of signal and idler modes in (10) does not grow exponentially in time, and thus the spectrum of excitations satisfies $\text{Im}(\omega_{\mathbf{k}}^{(i,\alpha,\ell)}) < 0$. When this condition is not met and there are values of $\mathbf{k}$ for which $\text{Im}(\omega_{\mathbf{k}}^{(i,\alpha,\ell)}) > 0$ for at least one of the branches, the pump-only solutions are dynamically unstable towards the exponential growth of these modes. The imaginary part of the excitation spectrum is plotted in the middle panels of Fig. 2 for two different values of the pump strength. As observed previously, there is a trivial contribution to the imaginary part of the spectrum coming from the decay terms: i.e., at large values of momenta, $\lim_{k\to\infty} \text{Im}(\omega_{\mathbf{k}}^{(i,\alpha,\ell)}) = -\kappa_\alpha$ (in the plot we have chosen $\kappa_X = \kappa_C$). However, for smaller values of momentum, the anomalous terms in the Bogoliubov matrix characterizing the coupling between the particle and hole degrees of freedom induce a nontrivial k-dependent contribution to $\text{Im}(\omega_{\mathbf{k}}^{(i,\alpha,\ell)})$. The region in momentum for which $\text{Im}(\omega_{\mathbf{k}}^{(i,\alpha,\ell)}) > 0$ characterizes the region of instability of the pump-only solutions. In Figs. 3 and 4, we plot the regions of instabilities as a function of momentum k and pump strength F_p. Because of the interaction between the two-pump states and thus the splitting of the LP and UP branches previously described, these regions of instability are characterized by separate regions or branches. Note that larger decay parameters κ_α imply smaller instability regions within the linear response analysis. Thus, even though it might seem desirable to have small values of κ_α so as to obtain large regions of instability, numerically, convergence of both two-pump and single-pump patterns occurs more quickly for larger values of κ_α. The choices reported in Table I as cases A and B are a compromise between these two tendencies.

The most unstable modes, i.e., those modes for which $\text{Im}(\omega_{\mathbf{k}}^{(i,\alpha,\ell)})$ is maximum as a function of $\mathbf{k}$, provide information about which mode is growing faster and, thus, about the expected momentum of the instability pattern. In the middle panels of Fig. 2 we indicate the most unstable modes as dotted (red) lines. The evolutions of the most unstable mode as a function of the pump strength are plotted also as dotted (red) lines in the top panels of both Figs. 3 and 4. There is a good agreement between these values of instability momenta and those previously obtained by estimating the renormalized LP and UP dispersions. Using the same style (and color) scheme of the bottom panels of Fig. 2, we plot in Figs. 3 and 4 as (cyan) dashed lines the expected momenta for the two-pump instability at $\omega_s = (\omega_{p_1} + \omega_{p_2})/2$ and as (green) dotted-dashed line those for the single-pump instability at ω_{p_1}. Note that, as a consequence of the assumed isotropy of the exciton-exciton interaction, the spectrum of excitation is also isotropic in momentum, i.e., $\omega_{\mathbf{k}}^{(i,\alpha,\ell)}$ only depends on $k = |\mathbf{k}|$. Thus, the most unstable modes only give information about the ring in momentum at which the instability can occur, but not about its direction. In other words, one cannot differentiate between stripe, checkerboard, or any other pattern. In order to obtain
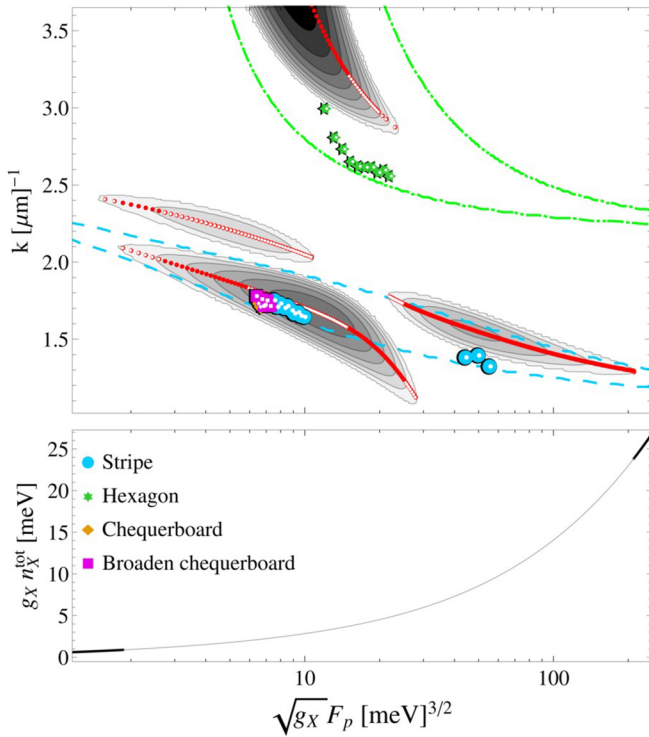
FIG. 3. Top panel: regions of instability of the pump-only solutions in the momentum k and pump strength F_p space. The contour plot represents the region of dynamical linear instability $\mathrm{Im}(\omega_{\mathbf{k}}^{(i,\alpha,\ell)}) > 0$. The estimates of the expected momenta for the two-pump instability at $\omega_s = (\omega_{p_1} + \omega_{p_2})/2$ [(cyan) dashed line] and for the single-pump instability at ω_{p_1} [(green) dotted-dashed line] are obtained as described in the bottom panels of Fig. 2. The dotted (red) lines indicate the most unstable modes as in the middle panels of Fig. 2: filled (red) dotted lines are those with the highest value of $\mathrm{Im}(\omega_{\mathbf{k}}^{(i,\alpha,\ell)}) > 0$. Symbols are the results of numerical simulations for finite-size pump spots as described later in Sec. IV. Bottom panel: evolution of the total excitonic population n_X^{tot} of the pump states as a function of the rescaled pump strength. For both panels, parameters are fixed as in the case A described in Table I. In this case, there is an interval in pump strength for which two- and single-pump instabilities compete against each other.

this information, we have to carry on a full numerical analysis, as discussed in the next section.

Finally, we note that in Fig. 3 (parameter choice A) there is a region in pump strength for which both two- and single-pump instabilities are allowed and compete against each other. As discussed in the next section, this competition between instabilities hinders the numerical convergence of the dynamics to a steady state. For this reason, the parameters of case B are chosen so as to eliminate the regions of single-pump instability, as shown in Fig. 4. The absence of competition between two- and single-pump instabilities leads to an easier convergence of patterns in the numerical simulations, which is what we are going to discuss in the next section.

IV. NUMERICAL ANALYSIS

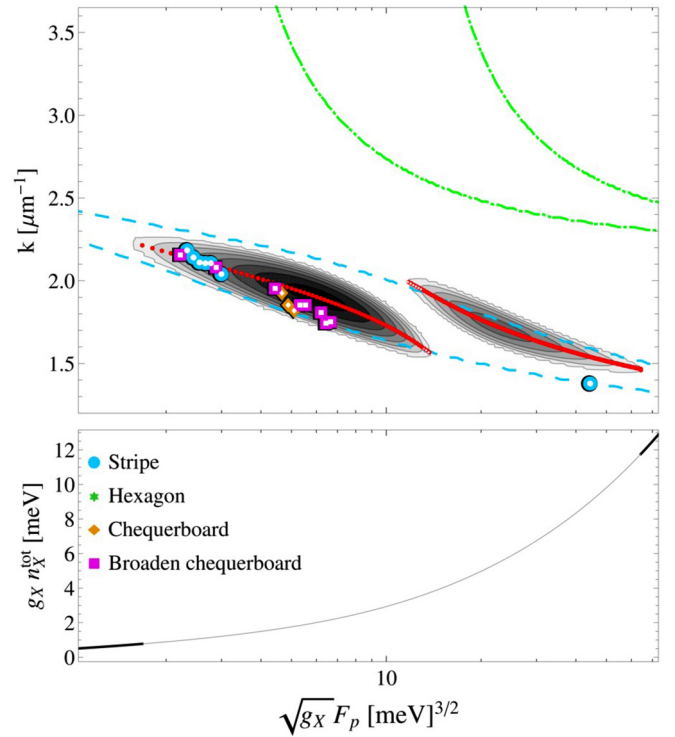As already mentioned in Sec. II A, the linear response analysis contains only the quadratic scattering processes

FIG. 4. Top and bottom panels are the same as in Fig. 3 but for the system parameters fixed as in the case B described in Table I. The parameters have been fixed so as to eliminate the region of instability corresponding to single-pump parametric scattering at the pump-1 energy ω_{p_1}. As discussed later, the absence of competition between two- and single-pump instabilities leads to an easier convergence of stripe and checkerboard patterns in the numerical simulations.

[see Fig. 1(c)]. As such, it allows to ascertain the stability of the pump-only solutions, and thus it provides us with the information about the region of system parameters for which we expect single- and two-pump instabilities to occur. However, a linear response analysis does not permit to deduce the specific patterns associated to each instability. For this reason, we carry on here a full numerical analysis of the generalized Gross-Pitaevskii equation (2) for finite-size pump spots (1). In particular, in order not to break the original rotational symmetry when both pumps are shined at normal incidence, we consider circularly symmetric smoothed top-hat profiles with a full width at half-maximum (FWHM) $\sigma_p \simeq 34\ \mu$m and a strength F_p (evaluated at the maximum value of the pump profile in real space). Note that, as already done for the linear response theory, also in the numerical simulations we rescale the two pump strengths according to (8) and thus we have a single pumping strength parameter F_p to be varied. In order to be able to compare the numerical results with those obtained from the linear response theory, we have chosen the same system parameters as in Table I, and, later on, we will report results for both parameter choices of cases A and case B. Equation (2) is numerically solved on a two-dimensional (2D) grid of $N \times N = 2^8 \times 2^8$ points and a separation of $0.32\ \mu$m, in a $L \times L = 81\ \mu$m $\times\ 81\ \mu$m box, by using a fifth-order adaptive-step Runge-Kutta algorithm. We have checked all our

TABLE II. Typical times required to reach a steady-state solution t_{sst} as a function of the white-noise variance σ_{noise}^2 of the initial conditions (14). These data refer to the system parameter choice B of Table I and correspond to the checkerboard pattern in Fig. 6.

σ_{noise}^2 (meV μm^2)	0.01	0.06	0.14	1.44	14.40
t_{sst} (ns)	473.4	220.9	99.9	42.1	36.8

results are converged with respect to the temporal and spatial resolution.

We impose white-noise random initial conditions with zero mean $\langle \psi_{\alpha=X,C}(\mathbf{r}, t=0) \rangle = 0$ and variance σ_{noise}^2:

$$g_X \langle \psi_\alpha^\dagger(\mathbf{r}, 0) \psi_{\alpha'}^\dagger(\mathbf{r}', 0) \rangle = \sigma_{noise}^2 \delta_{\alpha,\alpha'} \delta(\mathbf{r} - \mathbf{r}'). \quad (14)$$

This is a standard procedure done in order not to bias the steady-state solution selected by the dynamics. At the same time, random initial conditions introduce a small explicit breaking of the translational and rotational symmetries. This helps the numerics evolving towards solutions for which both symmetries are spontaneously broken, only when the system parameters are such that the symmetric pump-only solution is unstable. We let the dynamics evolve until a steady state, if any, is reached and select only those solutions that do reach a steady state. We have checked that none of our results depend on the choice of the initial conditions. We find that the specific value of the noise variance σ_{noise}^2 only affects the typical time t_{sst} the system needs to reach a steady state. In particular, larger values of σ_{noise}^2 typically lead to a faster convergence in time, as shown in Table II. This tendency of faster convergence in time for a stronger noise in the initial conditions is valid only for values of σ_{noise}^2 above a certain threshold. For a weaker noise, $\sigma_{noise}^2 < 0.01$ meV μm^2, we do not observe a monotonic behavior of t_{sst}. Finally, note that the orientation of each pattern is randomly selected. By fixing the system parameters and choosing a different realization of initial conditions, the system evolves exactly to the same pattern but with a different orientation.

As previously observed in Sec. III, larger values of the decay parameters κ_α tend to stabilize pump-only solutions and reduce the region of instability towards spontaneous pattern formation. However, from a numerical point of view, choosing too small values of the decay parameters hinders the stabilization of a determinate pattern to a steady-state regime. A compromise between these two behaviors has led us to the optimal values of κ_α reported in Table I.

Once the parameters are fixed as either in case A or case B of Table I, we scan through different values of the pump strength F_p and let the dynamics evolve until a steady state is reached for $t > t_{sst}$. As shown in Figs. 3 and 4, at either very low or very high pump powers, the only stable solutions are those where only the two-pump states at energies ω_{p_1} and ω_{p_2} are populated, and thus no pattern is generated. However, at intermediate pump strengths, we observe that the pump-only solutions are unstable towards the formation of either stripe, checkerboard, or hexagonal patterns. By filtering the emission at different energies, we will later be able to ascribe stripes and checkerboards to two-pump instabilities at an energy $\omega_s = (\omega_{p_1} + \omega_{p_2})/2$, while hexagonal patterns to one-pump instabilities only at an energy ω_{p_1}.
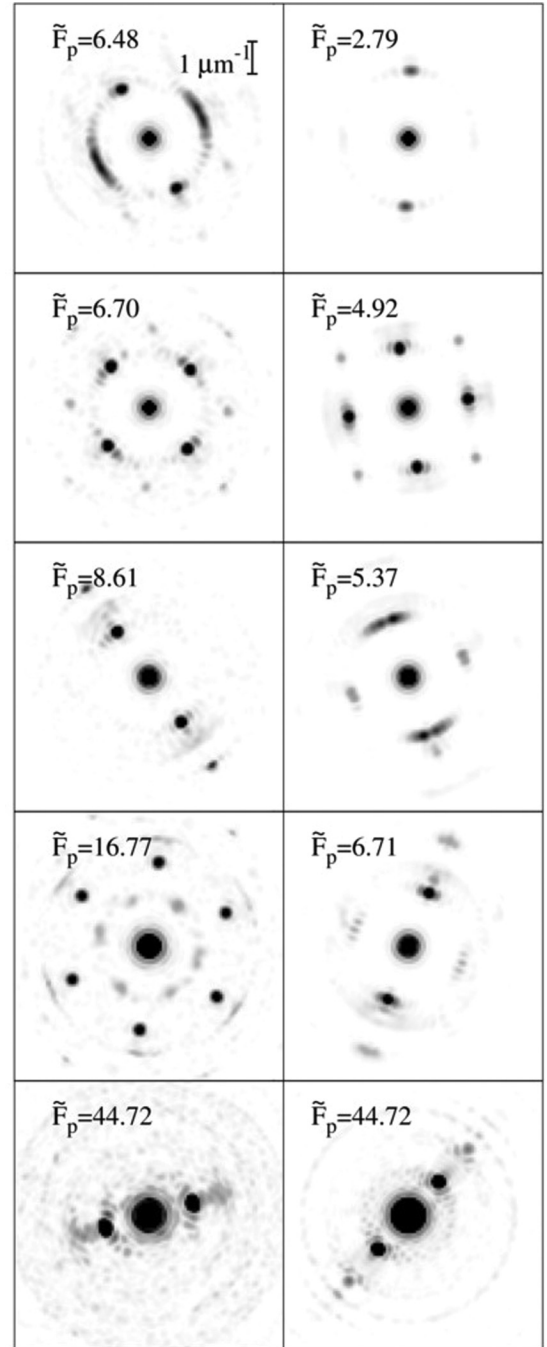

FIG. 5. Photon emission $|\psi_C(\mathbf{k}, t)|^2$ in reciprocal space $\mathbf{k}$ (μm^{-1} units) in the steady-state regime $t > t_{sst}$. System parameters are those of case A of Table I for the left column and case B for the right column, while the rescaled pump strength $\tilde{F}_p = \sqrt{g_X} F_p$ (meV$^{3/2}$ units) increases from the top panels to the bottom ones as indicated.

Typical stable steady-state patterns for different values of the pump strength are shown in Fig. 5, where we plot the full photon emission $|\psi_C(\mathbf{k}, t)|^2$ in momentum space $\mathbf{k}$ at a fixed time $t > t_{sst}$. Note that, plotting the emission at a given time implies an integration in energy, i.e., $\psi_C(\mathbf{k}, t) = \int d\omega \, e^{i\omega t} \psi_C(\mathbf{k}, \omega)$, and thus it includes the emission from all possible energy states, including both pump states as well as signal and idler states all emitting at different energies. In fact, we can appreciate that all the patterns in Fig. 5 include

emission around $\mathbf{k} = 0$ due to both pump states. Emission is broadened in momentum space because of the pumps being finite size; note that in some panels the broadening appears falsely increased because of the contour plot chosen interval. In addition to the emission at zero momentum, the emission at finite momentum characterizes different patterns. We can clearly distinguish in the patterns of Fig. 5 a dominant stronger emission on a momentum ring of radius k_{primary} and, in some of these panels, we can appreciate a secondary weaker emission on a different momentum ring $k_{\text{secondary}}$. As analyzed later, the origin of primary and secondary patterns can be easily explained by filtering the full emission at different energies.

For each pattern at a given pump strength F_p, we extract the value of the primary pattern momentum k_{primary} and we compare these numerical results with the results obtained within the linear response theory in Figs. 3 and 4. Here, the results from the numerical analysis are plotted as symbols. We can observe that stripe patterns occur at either low pump powers (as the panels of Fig. 5 corresponding to $\tilde{F}_p = 2.79$ meV$^{3/2}$, $\tilde{F}_p = 8.61$ meV$^{3/2}$, and $\tilde{F}_p = 6.71$ meV$^{3/2}$) or high pump powers (as for $\tilde{F}_p = 44.72$ meV$^{3/2}$). Instead, checkerboard patterns occur only at low pump powers (as for $\tilde{F}_p = 4.92$ meV$^{3/2}$ and $\tilde{F}_p = 6.70$ meV$^{3/2}$), including what we indicate as "broaden checkerboards" at $\tilde{F}_p = 6.48$ meV$^{3/2}$ and $\tilde{F}_p = 5.37$ meV$^{3/2}$. It is evident in both Figs. 3 and 4 that the primary pattern momentum k_{primary} we extract from the numerical simulations agrees extremely well with the lowest momentum branch of the most unstable modes extracted from the imaginary part of the excitation spectrum derived within the linear response theory. If no single-pump instability is allowed, as it happens for the parameter choice B of Fig. 4 and the right column of Fig. 5, the primary pattern momentum k_{primary} decreases monotonously as a function of the pump strength F_p. Here, there is no clear transition from stripe to checkerboard patterns, rather both instabilities alternate as the pump strength increases. However, if single-pump instabilities are allowed as for the parameter choice A of Fig. 3 and the left column of Fig. 5, at intermediate pump strengths, we observe the formation of hexagonal patterns. By filtering the emission in energy we can show that hexagonal patterns only occur at the energy ω_{p_1} of the pump which is tuned closer to the UP. Here, single- and two-pump instability compete against each other.

In order to show that different patterns can appear because of scattering processes at different energies, in Figs. 6, 7, and 8 we filter in energy the emission of typical checkerboard, stripe, and hexagonal patterns, respectively. To do this, in all these three figures we plot, in the top left panel, the photon spectrum integrated over the momentum angle $\mathcal{I}(k, \omega) = \int d\varphi |\psi_{\text{C}}(\mathbf{k}, \omega)|^2$, where $\mathbf{k} = (k, \varphi)$, versus the rescaled energy $\omega - \omega_{\text{X}, \mathbf{0}}$ and the absolute value of momentum k. On the right top panel we instead plot the momentum-integrated photon spectrum $\mathcal{I}_{\text{int}}(\omega) = \int d\mathbf{k} |\psi_{\text{C}}(\mathbf{k}, \varphi, \omega)|^2$. Here, we can observe that the emission in energy is deltalike peaked at energies equally spaced by $(\omega_{p_1} - \omega_{p_2})/2$: aside from the strong emission at the two-pump energies ω_{p_1} and ω_{p_2}, we can observe the emission at the signal energy $\omega_s = (\omega_{p_1} + \omega_{p_2})/2$ which is the energy characteristic of two-pump instabilities. In addition, we can appreciate a weak emission at one idler energy $\omega_{i_1} = (3\omega_{p_1} - \omega_{p_2})/2$, above the pump 1. The other idler energy
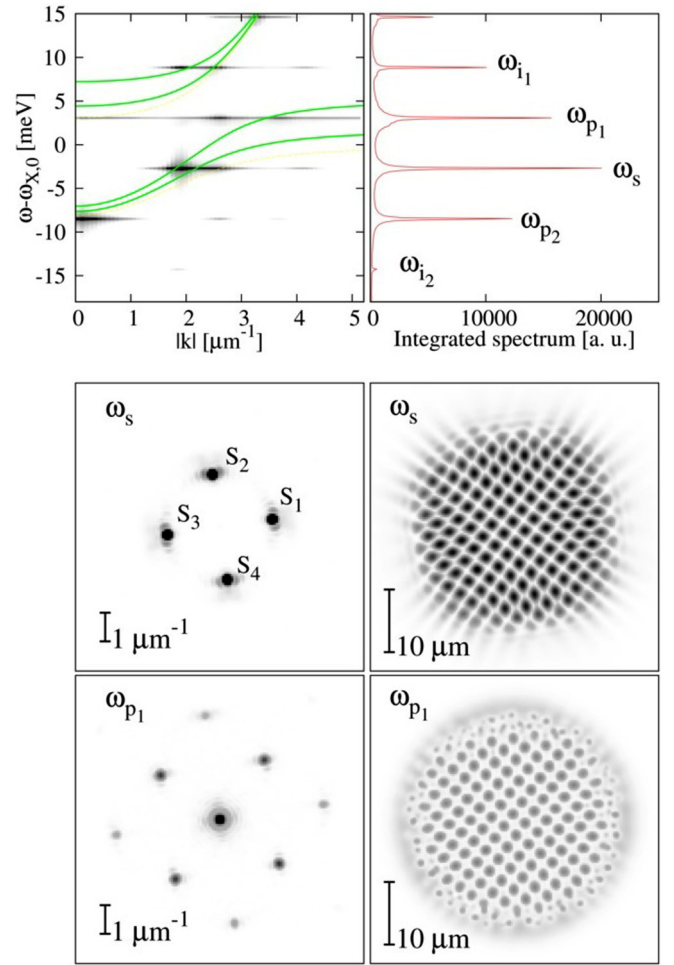

FIG. 6. Top left panel: photon spectrum integrated over the momentum angle $\mathcal{I}(k, \omega) = \int d\varphi |\psi_{\text{C}}(k, \varphi, \omega)|^2$ [(gray) contour plot]. The LP and UP dispersions renormalized and split because of interaction effects are plotted as (green) solid lines: these are obtained by diagonalizing the simplified Bogoliubov matrix (13). Top right panel: momentum-integrated photon spectrum $\mathcal{I}_{\text{int}}(\omega) = \int d\mathbf{k} |\psi_{\text{C}}(k, \varphi, \omega)|^2$. The four bottom panels represent the photon emission momentum (left) and space (right) profiles filtered at the energy of the signal $\omega_s = (\omega_{p_1} + \omega_{p_2})/2$ [top left $|\psi_{\text{C}}(\mathbf{k}, \omega_s)|^2$ and top right $|\psi_{\text{C}}(\mathbf{r}, \omega_s)|^2$] and at the energy of the pump-1 ω_{p_1} [bottom left $|\psi_{\text{C}}(\mathbf{k}, \omega_{p_1})|^2$ and top right $|\psi_{\text{C}}(\mathbf{r}, \omega_{p_1})|^2$]. System parameters are fixed to case B of Table I and the pump strength is $\tilde{F}_p = 4.92$ meV$^{3/2}$.

$\omega_{i_2} = (3\omega_{p_2} - \omega_{p_1})/2$, below pump 2, is extremely weakly populated because far from being in resonance to both the LP and the UP renormalized dispersions. This also happens to the additional satellite states equally spaced at a distance $(\omega_{p_1} - \omega_{p_2})/2$.

In all three Figs. 6, 7, and 8, in the bottom four panels, we filter the emission in energy at both the signal ω_s as well the pump-1 energy ω_{p_1} and plot the filtered emission both in momentum [left panels $|\psi_{\text{C}}(\mathbf{k}, \omega_s)|^2$ and $|\psi_{\text{C}}(\mathbf{k}, \omega_{p_1})|^2$] as well as in space [right panels $|\psi_{\text{C}}(\mathbf{r}, \omega_s)|^2$ and $|\psi_{\text{C}}(\mathbf{r}, \omega_{p_1})|^2$]. We observe that, for both cases of two-pump instabilities leading to checkerboards (Fig. 6) and stripes (Fig. 7), primary and secondary instabilities correspond to the same pattern even if at different absolute values of momenta and $k_{\text{primary}} < k_{\text{secondary}}$.
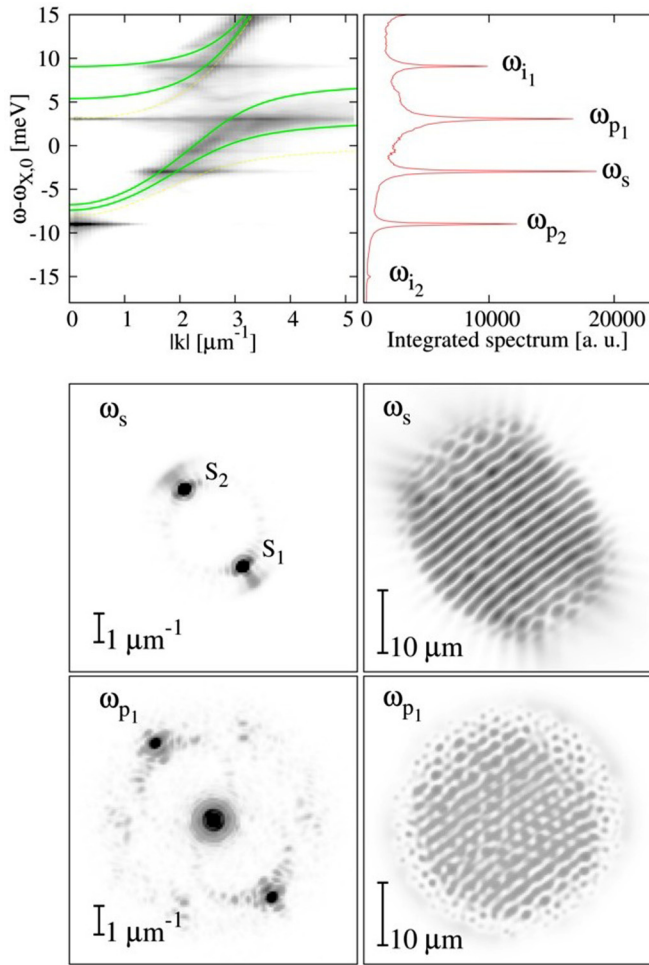
FIG. 7. Same as Fig. 6 for system parameters as case A of Table I and for a rescaled pump strength $\tilde{F}_p = 8.61$ meV$^{3/2}$.

FIG. 8. Same as Fig. 6 for system parameters as case A of Table I and for a rescaled pump strength $\tilde{F}_p = 16.77$ meV$^{3/2}$.

However, for single-pump instabilities such as the one in Fig. 8, we observe that primary and secondary patterns are not only characterized by a different absolute value of momentum and that $k_{\text{primary}} > k_{\text{secondary}}$, in addition they correspond to different pattern. The stronger emission in Fig. 8 is at the pump-1 energy and describes a hexagonal pattern with k_{primary}. From the spectrum plotted in the top left panel of Fig. 8, we can appreciate that k_{primary} is in very good agreement with the estimate we get from the renormalized LP dispersion (green) solid line. The emission at the signal energy ω_s is instead weaker and the filtered emission shows a distorted checkerboard with some weaker emission along the entire momentum ring of radius $k_{\text{secondary}}$.

A. Phase freedom

To conclude our study, we want to establish the phase freedom of two-pump instabilities. To do this, we first carry on an analytical study valid for homogeneous pumping. Later, we compare our analytical results with the numerical simulations for finite-size pumps.

Let us start from stripe patterns. In this case, the expansion (10) in signal ($S_{i\alpha}$) and idler ($I_{i\alpha}$) terms is limited to two opposite momentum states $\pm\mathbf{k}$:
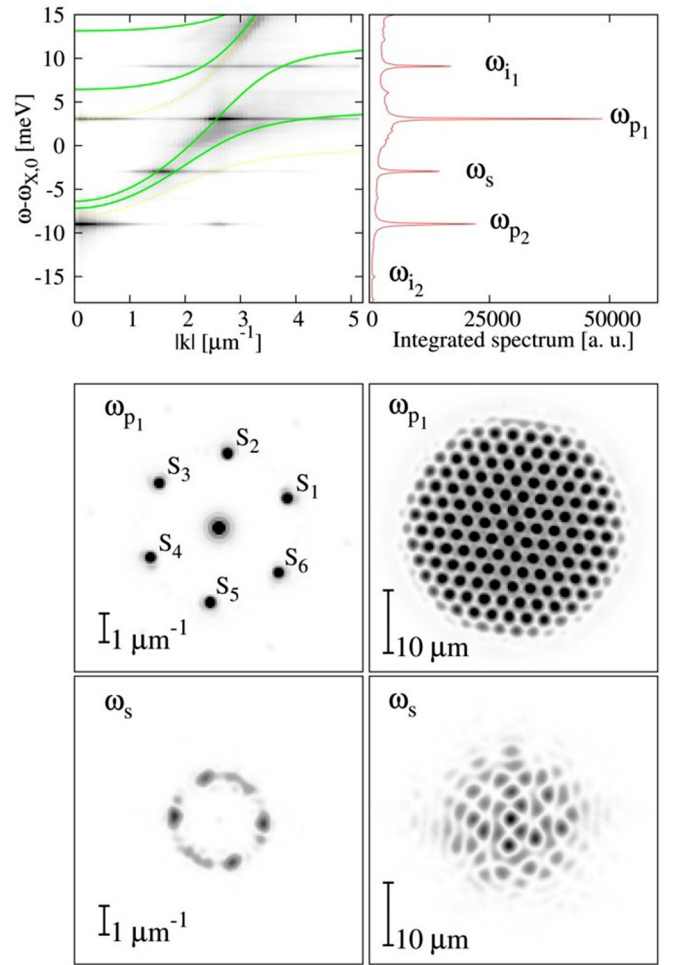
$$
\begin{aligned}
\psi_{\alpha,\text{stripe}}(\mathbf{r},t) = {} & e^{-i\omega_{p_1}t}P_{1\alpha} + e^{-i\omega_{p_2}t}P_{2\alpha} \\
& + e^{-i\omega_s t}[S_{1\alpha}^* e^{i\mathbf{k}\cdot\mathbf{r}} + S_{2\alpha}e^{-i\mathbf{k}\cdot\mathbf{r}}] \\
& + e^{-i\omega_{i_1}t}I_{1\alpha}e^{-i\mathbf{k}\cdot\mathbf{r}} + e^{-i\omega_{i_2}t}I_{2\alpha}^* e^{i\mathbf{k}\cdot\mathbf{r}}, \quad (15)
\end{aligned}
$$

where the signal energy is $\omega_s = (\omega_{p_1} + \omega_{p_2})/2$, while the two idler energies are $\omega_{i_1} = (3\omega_{p_1} - \omega_{p_2})/2$ and $\omega_{i_2} = (3\omega_{p_2} - \omega_{p_1})/2$. By substituting the expression for the stripe fields (15) into the equations of motion (2) and expanding to all orders, we can infer the constraints that have to be satisfied between the pump phases $\phi_{p_{1,2}}$ which are fixed externally and the signal $\phi_{s_{1,2}}$ and idler $\phi_{i_{1,2}}$ phases, where $P_{i\alpha} = |P_{i\alpha}|e^{i\phi_{p_i}}$, $S_{i\alpha} = |S_{i\alpha}|e^{i\phi_{s_i}}$, and $I_{i\alpha} = |I_{i\alpha}|e^{i\phi_{i_i}}$. Note that the $\alpha = $ X,C components have their phase locked to each other because of the Ω_R coupling in the equations of motion (2). We obtain that the scattering term (4) imposes only three independent constraints:

$$
\begin{aligned}
\phi_{p_1} + \phi_{p_2} &= \phi_{s_1} + \phi_{s_2}, \\
2\phi_{p_1} &= \phi_{s_1} + \phi_{i_1}, \\
2\phi_{p_2} &= \phi_{s_2} + \phi_{i_2}
\end{aligned}
$$

for the four phase terms $\phi_{s_{1,2}}$ and $\phi_{i_{1,2}}$. In fact, the constraint for the idler phases $\phi_{p_1} + \phi_{p_2} = \phi_{i_1} + \phi_{i_2}$ can be obtained by the above equations and it is not therefore independent from them. Thus, out of the four signal and idler phases, the system is free to spontaneously choose one relative phase only, e.g., either the relative phase between the two signals $\phi_{s_1} - \phi_{s_2}$ or the one between the two idlers $\phi_{i_1} - \phi_{i_2}$, and thus the stripe patterns are characterized by the spontaneous breaking of a U(1) phase symmetry.

We can carry on a similar analysis for the checkerboard solution, where we have now two pairs of opposite momenta states $\pm \mathbf{k}_1$ and $\pm \mathbf{k}_2$, resulting into four signal states $S_{1,2,3,4\alpha}$ (see notation of Fig. 6) and four idler states, two of which ($I_{1,4\alpha}$) at the energy ω_{i_1} and the other two ($I_{2,3\alpha}$) at the energy ω_{i_2}:

$$
\begin{aligned}
\psi_{\alpha,\text{check}}(\mathbf{r},t) \\
= e^{-i\omega_{p_1}t} P_{1\alpha} + e^{-i\omega_{p_2}t} P_{2\alpha} + e^{-i\omega_s t} \\
\times [S_{1\alpha}^* e^{i\mathbf{k}_1\cdot\mathbf{r}} + S_{3\alpha} e^{-i\mathbf{k}_1\cdot\mathbf{r}} + S_{2\alpha}^* e^{i\mathbf{k}_2\cdot\mathbf{r}} + S_{4\alpha} e^{-i\mathbf{k}_2\cdot\mathbf{r}}] \\
+ e^{-i\omega_{i_1}t} [I_{1\alpha} e^{-i\mathbf{k}_1\cdot\mathbf{r}} + I_{4\alpha}^* e^{i\mathbf{k}_2\cdot\mathbf{r}}] \\
+ e^{-i\omega_{i_2}t} [I_{2\alpha} e^{-i\mathbf{k}_2\cdot\mathbf{r}} + I_{3\alpha}^* e^{i\mathbf{k}_1\cdot\mathbf{r}}].
\end{aligned} \tag{16}
$$

Substituting into the equations of motion (2) we now obtain the following independent equations:

$$
\begin{aligned}
\phi_{p_1} + \phi_{p_2} &= \phi_{s_1} + \phi_{s_3}, \\
\phi_{p_1} + \phi_{p_2} &= \phi_{s_2} + \phi_{s_4}, \\
2\phi_{p_1} &= \phi_{s_1} + \phi_{i_1}, \\
2\phi_{p_2} &= \phi_{s_3} + \phi_{i_3}, \\
2\phi_{p_2} &= \phi_{s_2} + \phi_{i_2}, \\
2\phi_{p_1} &= \phi_{s_4} + \phi_{i_4}.
\end{aligned}
$$

We get six constraints for eight phases. The system thus spontaneously chooses two phases and is characterized by the spontaneous breaking of a U(1) × U(1) symmetry.

The phase freedom of hexagonal patterns due to single-pump instabilities was already derived in Ref. [6]. Here, one has a single-pump field oscillating at the energy ω_{p_1} and with phase ϕ_p, and six signal states, at the same energy as the pump, which we distinguish with an index h_j, with $j = 1, \ldots, 6$ (we assume the six signal states are arranged clockwise, see notation of Fig. 8). Now, the constraints for the phases read as

$$
2\phi_p = \phi_{h_j} + \phi_{h_{j+3}}, \quad \phi_p + \phi_{h_j} = \phi_{h_{j-1}} + \phi_{h_{j+1}}.
$$

One can easily check that out of these 12 equations only 4 are independent, thus again giving a U(1) × U(1) phase freedom, as in the case of the checkerboard pattern.

In order to confirm the phase freedom derived analytically for homogeneous pumping, we extract the signal phase profiles from the finite-size numerical results. Let us refer in particular to the case of the checkerboard pattern of Fig. 6, yet the same procedure can be applied to any pattern. We filter the emission at the signal energy in momentum space, evaluating $\psi_C(\mathbf{k},\omega_s)$. The amplitude of this field, for a checkerboard pattern, is peaked at four momenta $\mathbf{k}_{1,2,3,4}$, all arranged on the same ring k_{primary}. The phase profile $\phi_{s_{i=1,\ldots,4}}(\mathbf{r})$ associated to each of these
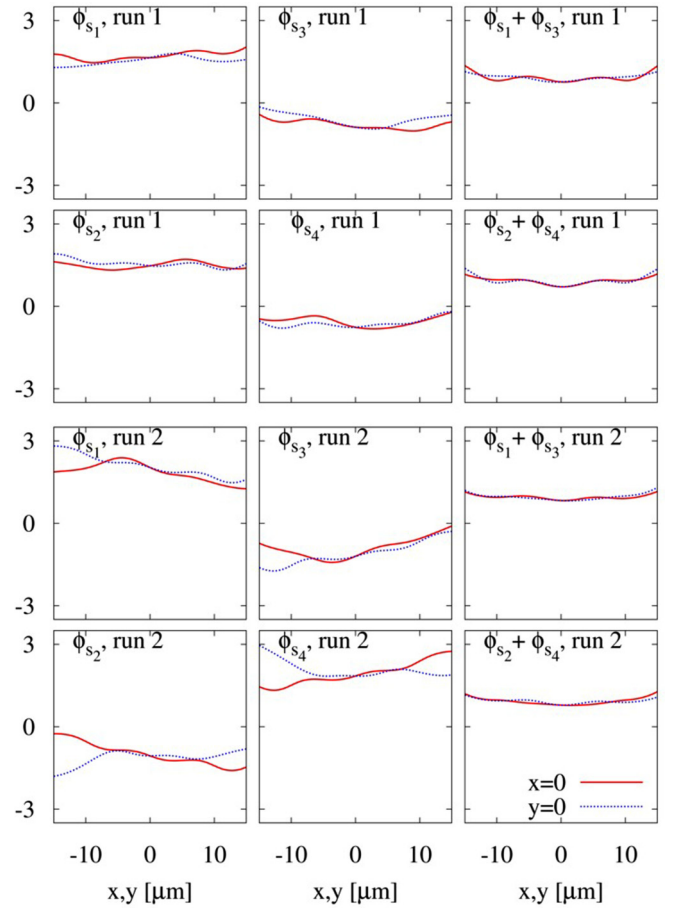

FIG. 9. First two columns: extracted signal phase profiles $\phi_{s_{1,2,3,4}}(\mathbf{r})$ of the four signal states for the same system parameters leading to the checkerboard pattern of Fig. 6 and for two different noise realizations of the random initial conditions (14) (labeled as run 1 and run 2). In particular, we plot the cut at $x = 0$ vs y [(red) solid line] and the cut at $y = 0$ vs x [(blue) dotted line]. Third column: we plot the sums $\phi_{s_1}(\mathbf{r}) + \phi_{s_3}(\mathbf{r})$ and $\phi_{s_2}(\mathbf{r}) + \phi_{s_4}(\mathbf{r})$ for the two runs in order to demonstrate the phase locking between them independently on the run.

four states can be extracted by evaluating

$$
\begin{aligned}
|\psi_{C,i}(\mathbf{r},\omega_s)| e^{\phi_{s_i}(\mathbf{r})} \\
= \sum_{\mathbf{k}} \psi_C(\mathbf{k},\omega_s)\theta(k_{\text{cut}} - |\mathbf{k} - \mathbf{k}_i|)e^{-i(\mathbf{k}-\mathbf{k}_i)\cdot\mathbf{r}},
\end{aligned} \tag{17}
$$

where we have chosen a momentum $k_{\text{cut}} \simeq 0.7$ mμ^{-1} for filtering the emission in momentum around the four signal momenta $\mathbf{k}_{i=1,\ldots,4}$. We plot the phase profiles $\phi_{s_{i=1,\ldots,4}}(x,y=0)$ and $\phi_{s_{i=1,\ldots,4}}(x=0,y)$ of the four signal states in Fig. 9 for the same system parameters leading to the checkerboard pattern of Fig. 6 and for two different noise realizations of the random initial conditions (14) (run 1 and run 2). Even though we have subtracted in Eq. (17) the leading current $\mathbf{k}_i$ to each phase profile, we can observe in all the panels of the first two columns of this figure that singularly all four phases $\phi_{s_i}(\mathbf{r})$ display a residual finite current $\mathbf{j}_{s_i}(\mathbf{r}) = -\nabla\phi_{s_i}(\mathbf{r}) \neq \mathbf{0}$ due to the system being finite size. However, we find that these residual currents are pairwise equal and opposite, i.e.,

$\mathbf{j}_{s_1}(\mathbf{r}) + \mathbf{j}_{s_3}(\mathbf{r}) \simeq \mathbf{0} \simeq \mathbf{j}_{s_2}(\mathbf{r}) + \mathbf{j}_{s_4}(\mathbf{r})$, so that the phase sums $\phi_{s_1}(\mathbf{r}) + \phi_{s_3}(\mathbf{r})$ and $\phi_{s_2}(\mathbf{r}) + \phi_{s_4}(\mathbf{r})$ shown in the panels of the last column are almost homogeneous in space. Further, we observe that $\phi_{s_1}(\mathbf{r}) + \phi_{s_3}(\mathbf{r}) \simeq \phi_{s_2}(\mathbf{r}) + \phi_{s_4}(\mathbf{r})$ within the same run, but also between different runs, i.e., for different random initial conditions. The fact the sums of these phases give the same value independently on the run we consider, while the phase of each singular phase $\phi_{s_i}(\mathbf{r})$ is different for different runs, demonstrates the phase locking between opposite momentum states, as well the spontaneous election of their phase difference, i.e., the pattern phase freedom.

The specific value of the phase sums $\phi_{s_1}(\mathbf{r}) + \phi_{s_3}(\mathbf{r}) = \phi_{s_2}(\mathbf{r}) + \phi_{s_4}(\mathbf{r})$ would be ideally zero, as they are equal to the sum of the two-pump phases. However, as the Fourier transform from time to frequency is evaluated numerically over a finite interval of time once the system has evolved long enough to reach a steady state, the filtering process in energy produces a fictitious numerical accumulated phase. This does not, however, influence our main conclusion about phase locking and phase freedom.

Note that, as we have extracted the signal state phases, we could similarly extract the idler phases so as to numerically check the phase locking between $\phi_{s_1} + \phi_{i_1}$, $\phi_{s_3} + \phi_{i_3}$, $\phi_{s_2} + \phi_{i_2}$, and $\phi_{s_4} + \phi_{i_4}$. However, the population of the idler states, particularly the ones at an energy $\omega_{i_2} = (3\omega_{p_2} - \omega_{p_1})/2$ below the pump-2 energy and below the LP dispersion, is so low to render the corresponding phases quite noisy and thus difficult to analyze. We have numerically extracted the phases of both stripe and hexagonal pattern and reached a similar conclusion about phase locking and phase freedom.

Finally, we would like to discuss here the experimental implications of the pattern phase freedom characterizing our proposed setup. Similarly to the optical parametric oscillator regime, phase freedom can be indirectly ascertained experimentally by questioning the persistency of flow via a pulsed Laguerre-Gauss beam as a diagnostic for superfluid behavior (see Refs. [24,25]). At the same time, if a vortex of, e.g., charge $m = +1$ is imprinted on one of the signal states (say S_1 of Figs. 6 and 7), then phase locking can be demonstrated by showing that the associated idler state (i.e., S_3 for a checkerboard in Fig. 6 and S_2 for a stripe in Fig. 7) spontaneously develops a vortex of opposite charge $m = -1$ at the same position. Further, the U(2) phase freedom of the checkerboard pattern implies that, even if the states S_1 and S_3 are characterized by a vortex of different charge, the other two signal states S_2 and S_4 keep their phase free of vortices, and thus are characterized by an independent phase.

In addition, our setup offers an interesting advantage over the broadly studied case of the optical parametric oscillator regime. In both cases, direct interference between one of the pumping lasers and one of the signal states cannot be performed because they emit at different frequencies. However, in our setup, signal states all emit at the same frequency. Thus, in the checkerboard configuration, the relative phase between the state S_1 and S_2 (see Fig. 6) can be measured by direct interference between the two signals after their emission is filtered in momentum.

V. CONCLUSIONS AND PERSPECTIVES

In this paper, we analyze the occurrence of Turing patterns in a polariton microcavity which is resonantly driven by two external lasers simultaneously pumping both lower and upper polariton branches. The pumps are shined at normal incidence so as not to explicitly break the system translational and rotational invariance. We show that, by increasing the intensity of both pumps, can lead to parametric scattering instabilities to signal states at finite momentum, thus spontaneously breaking the system translational and rotational symmetries. For two-pump instabilities, pumps and signals are at different energies, and we show that stripe and checkerboard patterns become the dominant steady-state solutions because cubic parametric scattering processes are forbidden. This contrasts with the case of single-pump instabilities, for which parametric scattering occurs at the same energy as one of the two pumps. In this case, it was already shown that hexagonal patterns are the most common instabilities [9–13]. We demonstrate that our setup allows two-pump instabilities to compete against single-pump instabilities, and that the system can simultaneously undergo different instabilities at different energies.

Our pumping setup has been previously suggested as a possible scheme for the generation of entangled multiple polariton modes [22]. In that work, it was assumed that parametric scattering would generate two signal states arranged into a stripe configuration. Taking into account the spin-polarization degrees of freedom, this would generate a total of four signal states, i.e., a square-type cluster state, for which four-mode entanglement was demonstrated. In our work, we analyze the nature and stability of different patterns that can emerge from two-pump instabilities. Already without taking into account the polarization degrees of freedom, we show that we can tune the system parameters so as to realize both stripe and checkerboard patterns. This would allow the realization of both four- and eight-mode polariton entanglement if the polarization degrees of freedom would be taken into account.

Further, by using the pump power as a tuning parameter, we have demonstrated that we can control the transition from stripe to checkerboard patterns. While stripes are characterized by the spontaneous breaking of a U(1) phase symmetry, in the case of checkerboard patterns, we show that the phase symmetry spontaneously broken is in the U(1) × U(1) class. We can thus tune the system across the nonequilibrium phase transition between these two states characterized by a different symmetry class. This opens intriguing questions about the critical behavior of this nonequilibrium two-dimensional system, and the nature of the transition from the normal phase to the ordered phase where the phase symmetry is spontaneously broken. It has been recently shown [27] that polaritons driven into the optical parametric oscillator steady-state regime undergo a transition from a normal to a superfluid phase [24] that is of the Berezinskii- Kosterlitz-Thouless type. The optical parametric oscillator regime is characterized by the spontaneous breaking of a U(1) phase symmetry. For this parametric scattering instability, it was shown that despite the presence of a strong drive and dissipation, the transition from the normal to the superfluid state is governed by the binding

and unbinding of vortex-antivortex pairs, sharing similarities to the equilibrium counterpart transition. It is therefore natural to ask whether our stripe pattern undergoes the same transition and to investigate the nature of the transition in the case of checkerboard patterns. These would be the subject of future studies.

To conclude, we would like to observe that our results apply to the case of clean microcavity heterostructures, where the effect of disorder both for photons and excitons is negligible. In our case, the broadening of exciton and photon lines is dominated by the homogeneous component, i.e., losses, rather than the inhomogeneous one. Studying the implications of disorder in pattern formation clearly goes beyond the scope of this work. Nevertheless, we can anticipate that sample disorder can provide a weak breaking of spatial homogeneity which might help stabilizing the orientation of stripe and checkerboard patterns and thus help their experimental observation.

APPENDIX: ANALOGY WITH WEAK CRYSTALLIZATION

It is interesting to note that there is some analogy between the spontaneous appearance of a determined pattern in polariton parametric scattering and the theory of weak localization [37,38]. The attempt to study the phase transition from a liquid to a crystal is notoriously a hard problem to analyze which goes back to Landau, as it implies the comparison between an infinite set of possible crystalline and quasicrystalline structures. However, a Ginzburg-Landau expansion in the density modulation order parameter $\psi(\mathbf{r})$ can be applied when the crystallization transition is weakly first order, greatly simplifying the problem. The resulting theory of weak crystallization assumes that the density modulations

$$\psi(\mathbf{r}) = \sum_{n=1}^{N} 2 \operatorname{Re}(a_n e^{i\mathbf{q}_n \cdot \mathbf{r}}) \qquad (A1)$$

are small and only select a single wave vector $|\mathbf{q}_n| = q_0$. The modulated pattern, whether stripe ($N = 1$), checkerboard ($N = 2$), hexagonal ($N = 3$), and so on, is found by minimiz-

ing a Ginzburg-Landau–type free-energy functional:

$$F[\psi] = \int d\mathbf{r} \left\{ \frac{\tau}{2} \psi^2 + \kappa \left[(\nabla^2 + q_0^2)\psi \right]^2 - \frac{\mu}{6} \psi^3 + \frac{\lambda}{24} \psi^4 \right\}.$$

In two dimensions, it is easy to show that in absence of the cubic term $\mu = 0$, there is a continuous transition from a liquid $\psi = 0$ phase for $\tau > 0$ to a stripe phase [$N = 1$, i.e., $\psi(\mathbf{r}) = 2|a_1| \cos(\mathbf{q}_1 \cdot \mathbf{r} + \Phi_1)$] for $\tau < 0$ with $|a_1| = \sqrt{2|\tau|/\lambda}$, where both phase Φ_1 and direction of $\mathbf{q}_1$ are randomly selected. However, in presence of the cubic term $\mu \neq 0$, which contributes if at least three vectors are arranged in $120°$, $\mathbf{q}_1 + \mathbf{q}_2 + \mathbf{q}_3 = \mathbf{0}$, the transition is to a 2D hexagonal crystal, $N = 3$, with $|a_1| = |a_2| = |a_3| = |\mu|[1 + \sqrt{1 - 10\lambda|\tau|/\mu^2}]/(5\lambda)$.

The free energy $F[\psi]$ is never minimized by a checkerboard $N = 2$ modulation. However, for two real order parameters

$$\psi_1(\mathbf{r}) = \sum_{n=1}^{N} 2 \operatorname{Re}(a_n e^{i\mathbf{q}_n \cdot \mathbf{r}}), \quad \psi_2(\mathbf{r}) = \sum_{m=1}^{M} 2 \operatorname{Re}(b_m e^{i\mathbf{p}_n \cdot \mathbf{r}}) ,$$
$$(A2)$$

with modulations in different directions $\mathbf{q}_n \neq \mathbf{p}_m$ but belonging to the same shell with momentum q_0, it can be shown that the free energy

$$F[\psi_1, \psi_2] = \int d\mathbf{r} \left\{ \sum_{i=1}^{2} \kappa_i \left[(\nabla^2 + q_0^2)\psi_i \right]^2 \right.$$
$$\left. + \frac{\tau}{2} (\psi_1^2 + \psi_2^2) + \frac{\lambda}{4} (\psi_1^2 + \psi_2^2)^2 + \gamma \psi_1^2 \psi_2^2 \right\}$$
$$(A3)$$

undergoes a transition for $\tau < 0$ from stripe $N = 1$, $M = 0$ when $\gamma > \lambda/4$ to checkerboard, $N = 1 = M$ when $-\lambda < \gamma < \lambda/4$.

Note that in the formulation above we have chosen real order parameters (A1) and (A2) rather than complex ones. This choice is dictated by the phase constraints discussed in Sec. IV A, where we have shown that the sum of signal phases corresponding to opposite momenta is locked to the pump phases. Note also that in its standard formulation with local interactions, the theory of weak crystallization selects randomly the directions $\mathbf{q}_i$ of the modulated phases. Thus, similarly to the case of our local interaction term (4), the weak crystallization theory does not distinguish between a checkerboard arranged in a square and the one arranged in a rhombus. However, this possibility can be phenomenologically added by including the dependence of the free energy on the angles between ordering wave vectors.

[1] A. V. Kavokin, J. J. Baumberg, G. Malpuech, and F. P. Laussy, *Microcavities* (Oxford University Press, Oxford, 2007).

[2] I. Carusotto and C. Ciuti, Rev. Mod. Phys. **85**, 299 (2013).

[3] D. Sanvitto and S. Kéna-Cohen, Nat. Mater. **15**, 1061 (2016).

[4] J. J. Baumberg, P. G. Savvidis, R. M. Stevenson, A. I. Tartakovskii, M. S. Skolnick, D. M. Whittaker, and J. S. Roberts, Phys. Rev. B **62**, R16247 (2000).

[5] C. Diederichs, J. Tignon, G. Dasbach, C. Ciuti, A. Lamaitre, J. Bloch, P. Roussignol, and C. Delalande, Nature (London) **440**, 904 (2006).

[6] P. Lewandowski, O. Lafont, E. Baudin, C. K. P. Chan, P. T. Leung, S. M. H. Luk, E. Galopin, A. Lemaître, J. Bloch, J. Tignon, P. Roussignol, N. H. Kwong, R. Binder, and S. Schumacher, Phys. Rev. B **94**, 045308 (2016).

[7] M. Abbarchi, V. Ardizzone, T. Lecomte, A. Lemaitre, I. Sagnes, P. Senellart, J. Bloch, P. Roussignol, and J. Tignon, Phys. Rev. B **83**, 201310 (2011).

[8] V. Ardizzone, M. Abbarchi, A. Lemaitre, I. Sagnes, P. Senellart, J. Bloch, C. Delalande, J. Tignon, and P. Roussignol, Phys. Rev. B **86**, 041301 (2012).

[9] H. Saito, T. Aioi, and T. Kadokura, Phys. Rev. Lett. **110**, 026401 (2013).

[10] M. H. Luk, Y. C. Tse, N. H. Kwong, P. T. Leung, P. Lewandowski, R. Binder, and S. Schumacher, Phys. Rev. B **87**, 205307 (2013).

[11] A. Werner, O. A. Egorov, and F. Lederer, Phys. Rev. B **89**, 245307 (2014).

[12] N. H. Kwong, C. Y. Tsang, S. M. H. Luk, Y. C. Tse, C. K. P. Chan, P. Lewandowski, P. T. Leung, S. Schumacher, and R. Binder, Phys. Scr. **92**, 034006 (2017).

[13] V. Ardizzone, P. Lewandowski, M. H. Luk, Y. C. Tse, N. H. Kwong, A. Lücke, M. Abbarchi, E. Baudin, E. Galopin, J. Bloch, A. Lemaitre, P. T. Leung, P. Roussignol, R. Binder, J. Tignon, and S. Schumacher, Sci. Rep. **3**, 3016 (2013).

[14] R. Hivet, E. Cancellieri, T. Boulier, D. Ballarini, D. Sanvitto, F. M. Marchetti, M. H. Szymanska, C. Ciuti, E. Giacobino, and A. Bramati, Phys. Rev. B **89**, 134501 (2014).

[15] T. Boulier, H. Terças, D. D. Solnyshkov, Q. Glorieux, E. Giacobino, G. Malpuech, and A. Bramati, Sci. Rep. **5**, 9230 (2015).

[16] C. E. Whittaker, B. Dzurnak, O. A. Egorov, G. Buonaiuto, P. M. Walker, E. Cancellieri, D. M. Whittaker, E. Clarke, S. S. Gavrilov, M. S. Skolnick, and D. N. Krizhanovskii, Phys. Rev. X **7**, 031033 (2017).

[17] J. O. Hamp, A. K. Balin, F. M. Marchetti, D. Sanvitto, and M. H. Szymańska, Europhys. Lett. **110**, 57006 (2015).

[18] A. Amo, S. Pigeon, D. Sanvitto, V. G. Sala, R. Hivet, I. Carusotto, F. Pisanello, G. Leménager, R. Houdré, E. Giacobino, C. Ciuti, and A. Bramati, Science **332**, 1167 (2011).

[19] F. R. S. A. M. Turing, Philos. Trans. R. Soc., B **237**, 37 (1952).

[20] M. C. Cross and P. C. Hohenberg, Rev. Mod. Phys. **65**, 851 (1993).

[21] K. Staliunas and V. Sánchez-Morcillo, *Transverse Patterns in Nonlinear Optical Resonators*, Springer Tracts in Modern Physics, Vol. 183 (Springer, Berlin, 2003).

[22] T. C. H. Liew and V. Savona, Phys. Rev. A **84**, 032301 (2011).

[23] T. C. H. Liew and Y. G. Rubo, Phys. Rev. B **97**, 041302 (2018).

[24] D. Sanvitto, F. Marchetti, M. Szymańska, G. Tosi, M. Baudisch, F. Laussy, D. Krizhanovskii, M. Skolnick, L. Marrucci, A. Lemaitre, J. Bloch, C. Tejedor, and L. Viña, Nat. Phys. **6**, 527 (2010).

[25] F. M. Marchetti, M. H. Szymańska, C. Tejedor, and D. M. Whittaker, Phys. Rev. Lett. **105**, 063902 (2010).

[26] A. C. Berceanu, L. Dominici, I. Carusotto, D. Ballarini, E. Cancellieri, G. Gigli, M. H. Szymańska, D. Sanvitto, and F. M. Marchetti, Phys. Rev. B **92**, 035307 (2015).

[27] G. Dagvadorj, J. M. Fellows, S. Matyjaśkiewicz, F. M. Marchetti, I. Carusotto, and M. H. Szymańska, Phys. Rev. X **5**, 041028 (2015).

[28] T. C. H. Liew and V. Savona, New J. Phys. **15**, 025015 (2013).

[29] O. Kyriienko and T. C. H. Liew, Phys. Rev. B **93**, 035301 (2016).

[30] C. Ciuti, P. Schwendimann, and A. Quattropani, Semicond. Sci. Technol. **18**, S279 (2003).

[31] I. Carusotto and C. Ciuti, Phys. Rev. Lett. **93**, 166401 (2004).

[32] A. Baas, J.-P. Karr, M. Romanelli, A. Bramati, and E. Giacobino, Phys. Rev. B **70**, 161307 (2004).

[33] Y. Sun, P. Wen, Y. Yoon, G. Liu, M. Steger, L. N. Pfeiffer, K. West, D. W. Snoke, and K. A. Nelson, Phys. Rev. Lett. **118**, 016602 (2017).

[34] D. M. Whittaker, Phys. Rev. B **71**, 115301 (2005).

[35] E. Cancellieri, F. M. Marchetti, M. H. Szymańska, and C. Tejedor, Phys. Rev. B **83**, 214507 (2011).

[36] E. Cancellieri, F. M. Marchetti, M. H. Szymańska, D. Sanvitto, and C. Tejedor, Phys. Rev. Lett. **113**, 169902(E) (2014).

[37] S. A. Brazovsky, I. E. Dzyaloshinsky, and A. R. Muratov, Zh. Eksp. Teor. Fiz. **93**, 1110 (1987) [Sov. Phys. JETP **66**, 625 (1987)].

[38] E. Kats, V. Lebedev, and A. Muratov, Phys. Rep. **228**, 1 (1993).